Supplementary Materials

Strain-modulation and enhancement of superconductivity in flexible $YBa_2Cu_3O_7$ thin films

Zelong Wang[1,#], Bingwen Liu[2,#], Dekun Shen[2,#], Xiaoyuan Zhou[3], Danfeng Li[4], YuJie Sun[5], Mingming Li[7], Bin Zhang[3], Chi Ho Wong[6], Jinxing Zhang[2], Ji-Yan Dai[1]

[1]Department of Applied Physics, The Hong Kong Polytechnic University, Hong Kong 999077, China.
[2]Department of Physics, Beijing Normal University, Beijing 100875, China.
[3]College of Physics and Institute of Advanced Interdisciplinary Studies, Chongqing University, Chongqing 400044, China.
[4]Department of Physics, City University of Hong Kong, Hong Kong 999077, China.
[5]Department of Physics, Southern University of Science and Technology, Shenzhen 518055, Guangdong, China.
[6]Division of Science, Engineering, and Health Studies, The School of Professional Education and Executive Development, The Hong Kong Polytechnic University, Hong Kong 999077, China.
[7]Key Laboratory of Materials Physics, Ministry of Education, School of Physics, Zhengzhou University, Zhengzhou 450001, Henan, China.
[#]These authors contributed equally to this work.

Correspondence to: Prof. Ji-Yan Dai, Department of Applied Physics, The Hong Kong Polytechnic University, Hong Kong 999077, China. E-mail: jiyan.dai@polyu.edu.hk; Prof. Jinxing Zhang, Department of Physics, Beijing Normal University, Beijing 100875, China. E-mail: jxzhang@bnu.edu.cn; Assoc. Prof. Bin Zhang, College of Physics and Institute of Advanced Interdisciplinary Studies, Chongqing University, Chongqing 400044, China. E-mail: xinyun2017@cqu.edu.cn; Chi Ho Wong, Division of Science, Engineering, and Health Studies, The School of Professional Education and Executive Development, The Hong Kong Polytechnic University, Hong Kong 999077, China. roy.wong@cpce-polyu.edu.hk

Supplementary Figure 1 shows that the film still has a large size after peeling, and there are no tiny cracks in the film, which is also an important reason why the stress cannot be completely released. This provides the basis for subsequent macro-level characterization of stress variations and differences in superconducting properties.

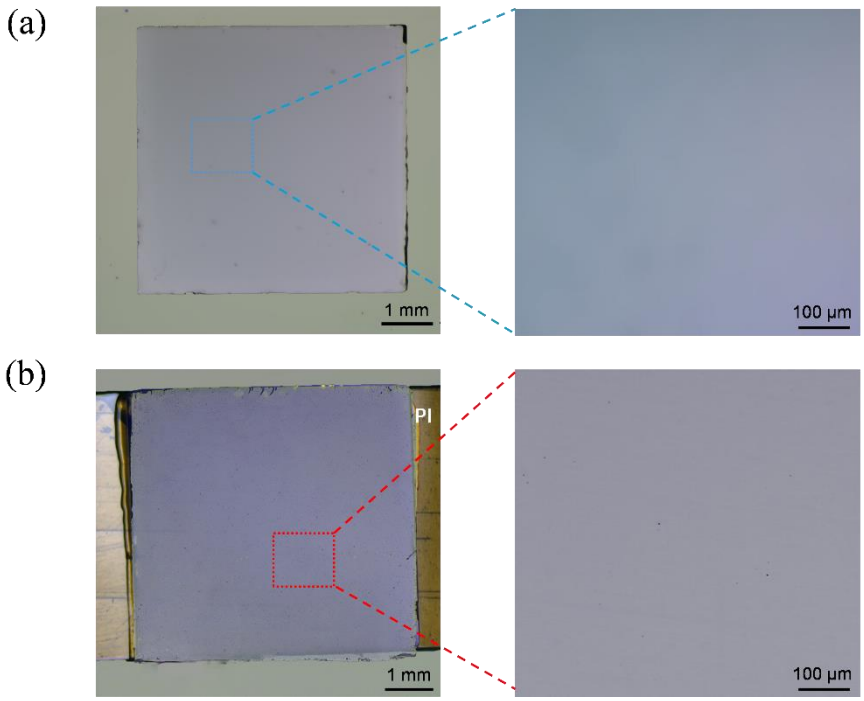

Supplementary Figure 1. Optical microscope images of YBCO thin films: (a) YBCO/STO/SAO/STO structure before peeling; (b) YBCO/PI structure after peeling. The corresponding magnified images show the integrity of the films.

Supplementary Figure 2 presents the Energy Dispersive Spectrometer (EDS) analysis and diffraction results obtained from STEM. Combined with EDS elemental mapping, the distribution of elements across different interfaces shows no intermixing or interdiffusion, confirming the high quality and sharpness of the interfaces. Meanwhile, diffraction patterns from the $YBa_2Cu_3O_7$ and $Sr_4Al_2O_7$ layers reveal distinct periodic arrangements, corresponding precisely to their respective crystal phases and structures. The sharp, well-defined diffraction patterns are indicative of high-quality thin-film crystallinity.

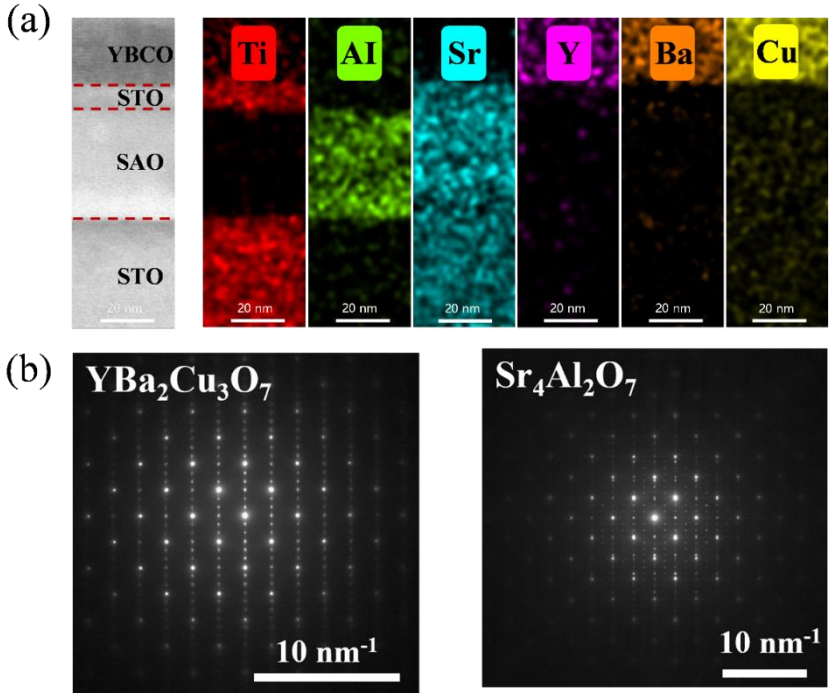

Supplementary Figure 2. (a) Cross-sectional EDS elemental mapping of the YBCO/STO/SAO/STO heterostructure. (b) Selected-area electron diffraction patterns obtained from distinct interfacial regions, corresponding to the $YBa_2Cu_3O_7$ (YBCO) and $Sr_4Al_2O_7$ (SAO) crystal phases, respectively.

Supplementary Figure 3 shows the results of different structures XRD test results and Williamson-Hall (WH) analysis. It can be seen that the characteristic peaks of thin films with the same structure but different thicknesses are almost identical and the characteristic peaks of YBCO/PI structure after peeling are very clean with no impurity peaks.

The WH fitting formula relates the peak broadening to both crystallite size (D) and micro-strain (ε_i) through the linear equation:

$$\beta\cos(\theta) = \frac{K\lambda_w}{D} + 4\varepsilon_i \sin(\theta),$$

where $\beta = \beta_{measured} - \beta_{instrument}$, $\beta_{measured}$ is the experimentally measured full width at half maximum (FWHM) of the thin film diffraction peak, $\beta_{instrument}$ is the broadening of the diffraction peak caused by the XRD instrument itself. For the YBCO/PI samples after exfoliation, the instrumental broadening (instrument) was determined by measuring the FWHM of the (00l) (l = 1,2,3) diffraction peaks from the single-crystal $SrTiO_3$ substrate. The intrinsic film FWHM (measured) was then obtained directly from the YBCO (003), (006), and (009) peaks in the released films. For the

YBCO/STO/SAO/STO heterostructure, due to the STO substrate peaks overlapping with the YBCO sample peaks, the FWHM of the YBCO sample peaks, which are near the STO characteristic peak, was selected to subtract the FWHM of STO for correction. The WH analysis results are plotted in Supplementary Figure 3b, showing the fitted curves [4sin(θ) vs βcos(θ)] for films of varying thicknesses before and after peeling, where the slope represents the inhomogeneous strain (ε_i) of the film.

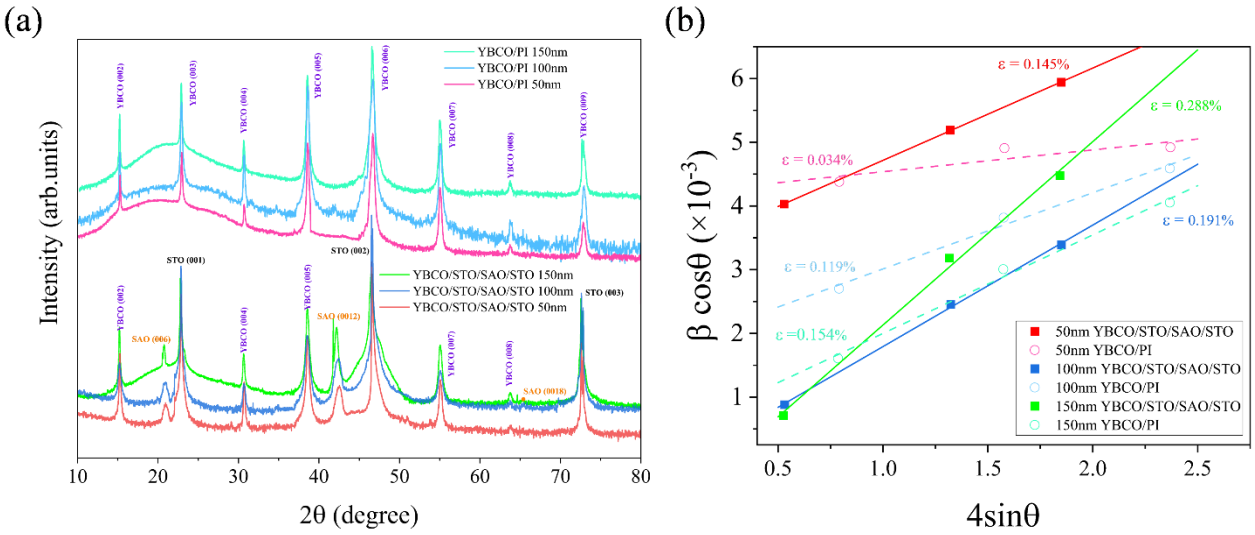

Supplementary Figure 3. (a)XRD test results before and after peeling of YBCO thin films with different thicknesses. The above is the YBCO/PI structure films after peeling, and the below is the YBCO/STO/SAO/STO structure. (b) Out-of-plane Williamson-Hall plot analysis for strain gradients before and after peeling for YBCO thin films of different thicknesses. The solid lines represent the fitted curves before peeling, and the dashed lines represent the fitted curves after peeling.

Supplementary Figure 4 presents the room-temperature micro-Raman spectroscopy results for YBCO thin films before and after the lift-off process, used to assess oxygen stoichiometry. The analysis focuses on the apical O(4) oxygen mode near 500 cm^{-1}, which is particularly sensitive to the oxygen content in $YBa_2Cu_3O_7$. For the freestanding YBCO/PI film after lift-off (Supplementary Figure 4a), a clearly resolved O(4) mode is observed at 501.1 ± 0.8 cm^{-1}, corresponding to an oxygen content close to $YBa_2Cu_3O_{6.96}$, indicating that the freestanding film remains near the optimally oxygenated YBCO phase. For the YBCO/STO/SAO/STO heterostructure before lift-off (Supplementary Figure 4b), the O(4) mode is not resolved as a sharp isolated peak due to the multilayer background. After local base subtraction in the 410-530 cm^{-1} range, a weak O(4)-like shoulder is resolved near 507.2 cm^{-1} (Supplementary Figure 4d), and including this shoulder

significantly improves the local fit (ΔAIC = -48.4). The relative blue shift in the O(4) mode for the substrate-bound film is attributed to the shortening of the Cu-O(4) bond along the c-axis under compressive strain; upon transfer, the epitaxial constraints are reduced, leading to strain relaxation and a red shift back toward the normal frequency, consistent with the XRD results. These Raman data confirm that the transfer process does not induce large-scale changes in oxygen stoichiometry, ruling out oxygen variation as the cause of the observed T^c enhancement.

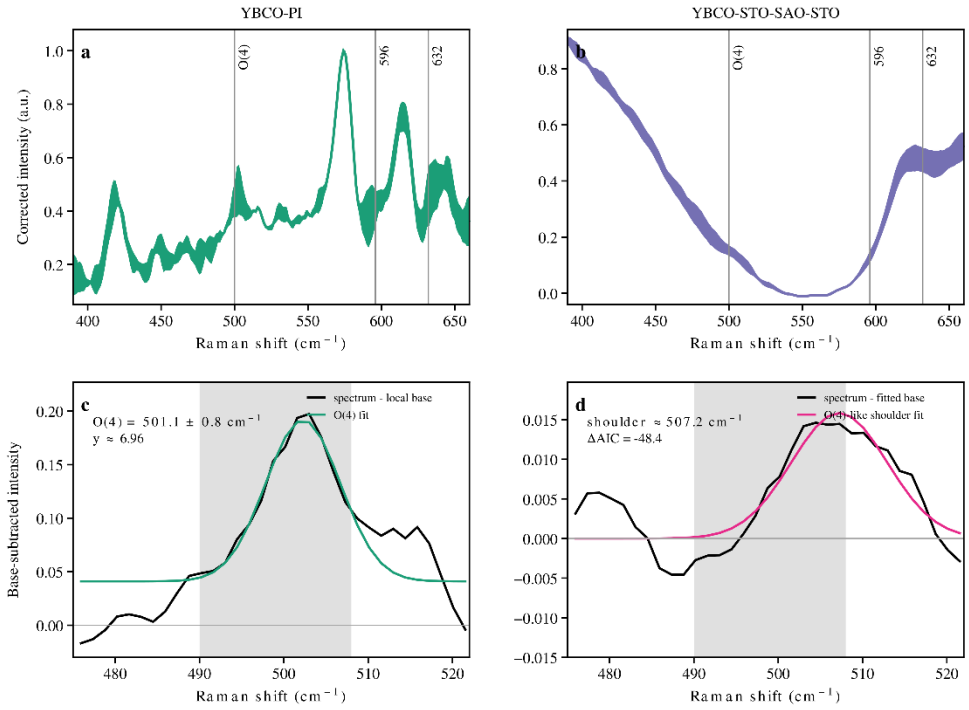

Supplementary Figure 4. Room-temperature micro-Raman analysis of the apical O(4) oxygen mode in YBCO before and after lift-off. (a) Raman spectrum of the freestanding YBCO/PI film after lift-off. (b) Raman spectrum of the YBCO/STO/SAO/STO heterostructure before lift-off. (c) Local base-subtracted spectrum of the freestanding YBCO/PI film in the O(4)-mode region; fitting gives a peak position of 501.1 ± 0.8 cm^{-1}. (d) Local base-subtracted spectrum of the YBCO/STO/SAO/STO heterostructure; a weak O(4)-like shoulder is resolved near 507.2 cm^{-1} (ΔAIC = -48.4), indicating the presence of the apical oxygen Raman contribution.

Supplementary Figure 5 displays the temperature-dependent resistance of the film, measured before and after exfoliation, under different magnetic fields. As the magnetic field strength increases, the transition temperature and the zero-resistance temperature are both systematically suppressed.

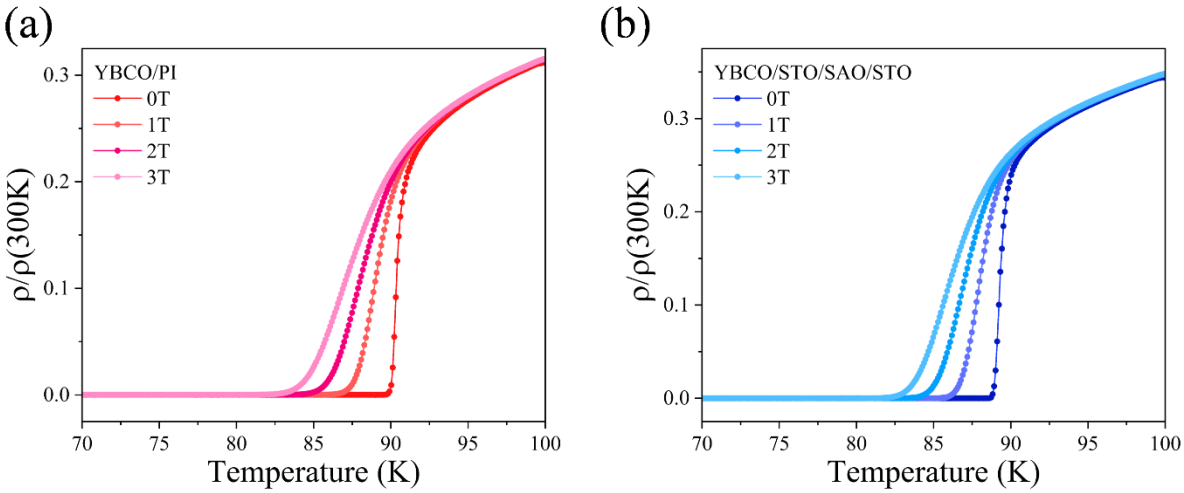

Supplementary Figure 5. Resistance-temperature changes under different magnetic field conditions: (a) YBCO/PI structure; (b) YBCO/STO/SAO/STO structure.

Supplementary Figure 6 presents the transport critical current density (J^c) characterization at 77 K for YBCO films before and after the transfer process. The resistance as a function of current density (R-J curves) measured at 77 K for the YBCO/STO/SAO/STO heterostructure and the transferred flexible YBCO/PI film exhibit nearly identical behavior. Using a standard voltage criterion, the extracted J^c at 77 K remains approximately 1.1×10^6 A/cm^2 for both structures, with negligible change after transfer. This overlapping behavior and well-preserved J^c provide compelling evidence that the substrate removal and transfer process is non-destructive, successfully avoiding the introduction of macroscopic cracks, severe mechanical peeling damage, or structural degradation that would otherwise severely depress the current-carrying capability. This robust transport performance, combined with the elevated T^c, underscores the immense potential of the flexible YBCO films for practical superconducting applications.

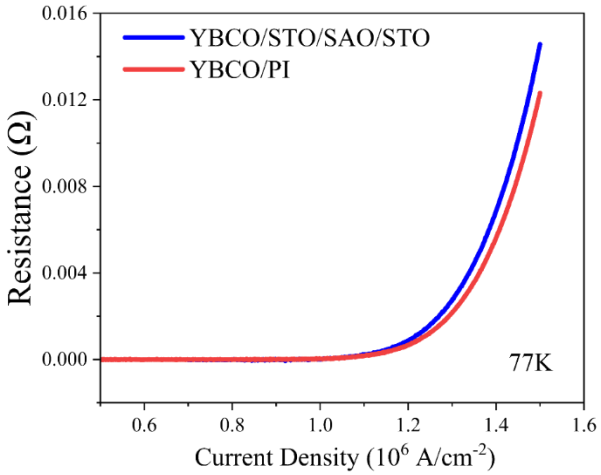

Supplementary Figure 6. Transport critical current density characterization at 77 K. Resistance as a function of current density (R-J curves) measured at 77 K for the YBCO/STO/SAO/STO heterostructure (blue curve) and the transferred flexible YBCO/PI film (red curve). The nearly identical tracking of the two curves demonstrates that the non-destructive transfer process preserves the intrinsic high current-carrying capability and structural integrity of the YBCO film, with $J^c \approx 1.1\times10^6$ A/cm² for both structures.

Supplementary Figure 7 presents schematics, photographs, and test data obtained from the independently developed TCMI test apparatus. Supplementary Figure 7(a) illustrates the overall measurement configuration, with an enlarged view on the right highlighting the test area. The corresponding physical realization of the PCB-integrated coil assembly is shown in Supplementary Figure 7(b). The core components, the drive coil and receive coil, were fabricated using 20-μm oxygen-free copper enameled wire, with dimensions of 1.3 mm in diameter and 1.6 mm in height. The spacing between the excitation and induction coils was set to 1.0 mm. Supplementary Figure 7(c) and (d) shows the temperature and time evolution of the real component (V_x) and imaginary component (V_y) of the mutual inductance signal for the sample before and after exfoliation. Both samples before and after peeling exhibit sharp transitions in the real component (Vx) and corresponding well-defined peaks in the imaginary component (Vy) within the transition temperature range, with relatively narrow full width at half maximum. These features collectively indicate that both samples have high superconducting quality.

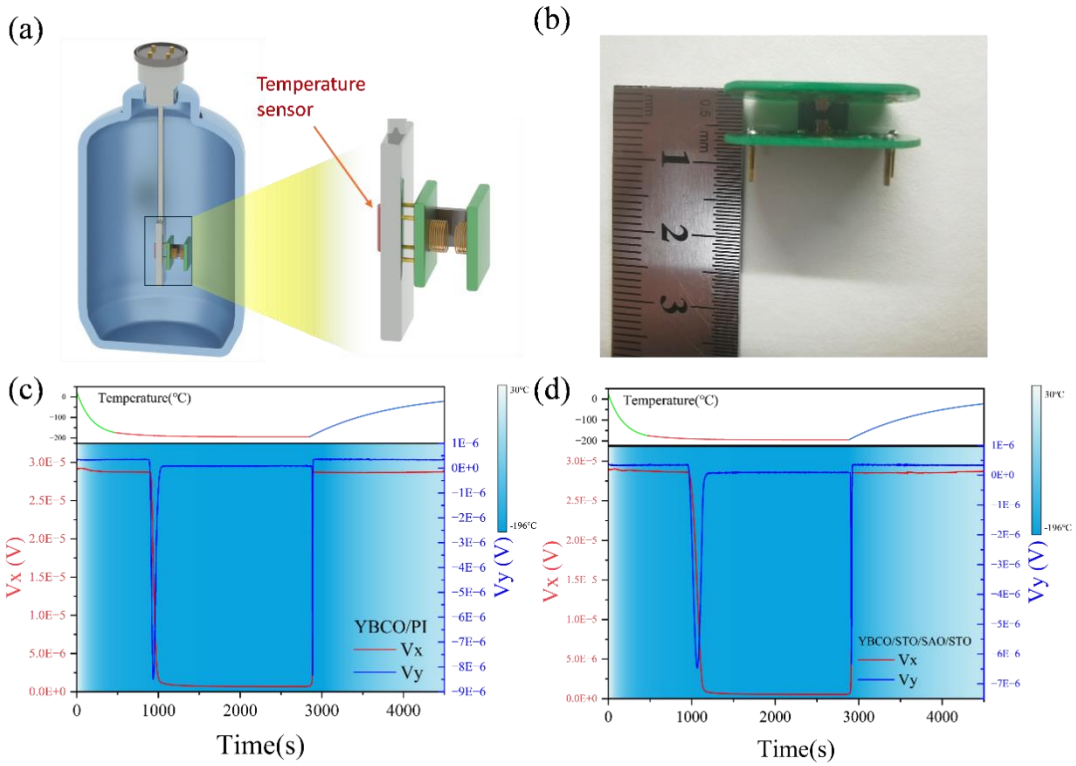

Supplementary Figure 7. (a) Schematic diagram of the self-built two-coil mutual inductance measurement system. The coil unit is inserted into the test rod via electrode pins and placed within a Dewar flask containing sufficient liquid nitrogen for variable-temperature testing. Temperature sensed by a Pt100 platinum resistance temperature sensor on the rod's back. (b) Photograph of the self-built two-coil mutual inductance device. Real component Vx(t) (red) and imaginary component Vy(t) (blue) of the induced voltage curve measured by the two-coil mutual inductance method for YBCO thin films. (c) YBCO/PI independent structure. (d) YBCO/STO/SAO/STO structure.

Supplementary Figure 8 presents optical microscopy images documenting the surface condition of the flexible YBCO film before and after a complete bending cycle, providing direct evidence for the crack-free nature of the bending process. The flexible thin film undergoes sequential tensile and compressive deformation. Optical microscopy images (scale bar: 100 μm) were captured at the initial and final states to examine the surface condition. The micrographs reveal that the YBCO film surface remains highly intact after a complete bending cycle, with no observable new cracks or structural damage, demonstrating excellent bendability and mechanical integrity of the flexible YBCO film. These results confirm that even under large applied bending strains, the film retains its structural integrity throughout the cyclic bending process.

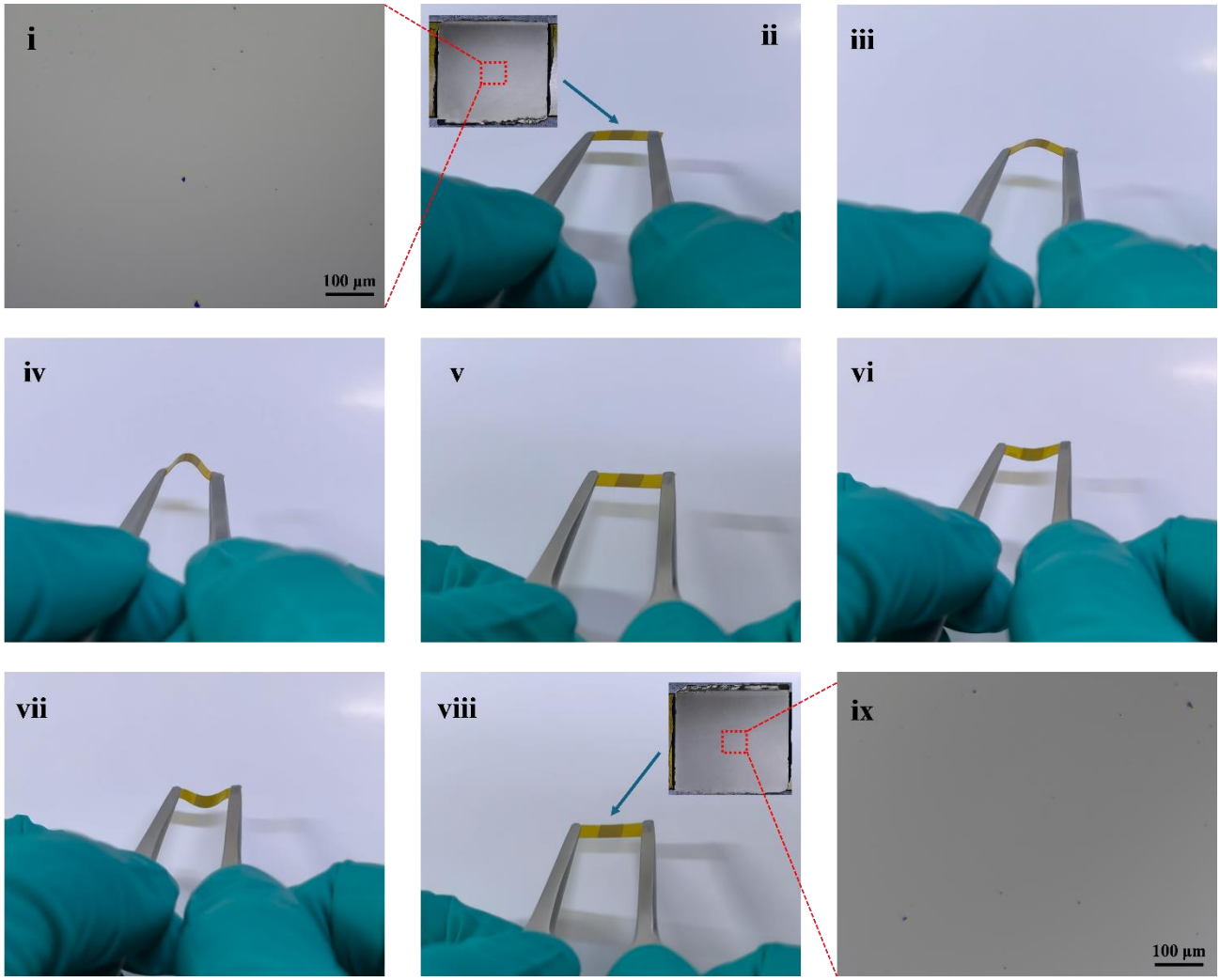

Supplementary Figure 8. Bending process and surface optical microscope photographs of flexible YBCO film. The flexible thin film undergoes sequential tensile (iii-iv) and compressive (vi-vii) deformation. Optical microscopy images (scale bar: 100 μm) were captured at the initial (i, ii) and final (viii, ix) states to examine the surface condition. The micrographs reveal that the YBCO film surface remains highly intact after a complete bending cycle, with no observable new cracks or structural damage, demonstrating excellent bendability and mechanical integrity of the flexible YBCO film.

Supplementary Figure 9 presents the results of three-cycle reproducibility testing of the flexible YBCO film under repeated bending conditions, providing statistical validation of the strain-dependent superconducting behavior. Supplementary Figure 9(a) shows the resistivity-temperature (80-100 K) curves of the flexible YBCO film under different bending states across three consecutive mounting-demounting cycles. The resistive behavior exhibits a high degree of reproducibility across all bending conditions. Supplementary Figure 9(b) presents the average transition temperature T_c and

zero-resistance temperature T_0 obtained from each bending condition, with error bars representing the standard deviation from the three-cycle tests. The standard deviation is substantially smaller than the T^c change induced by bending, confirming the statistical significance of the strain-dependent modulation. These results also indirectly confirm that the YBCO film does not sustain mechanical damage under repeated cyclic bending.

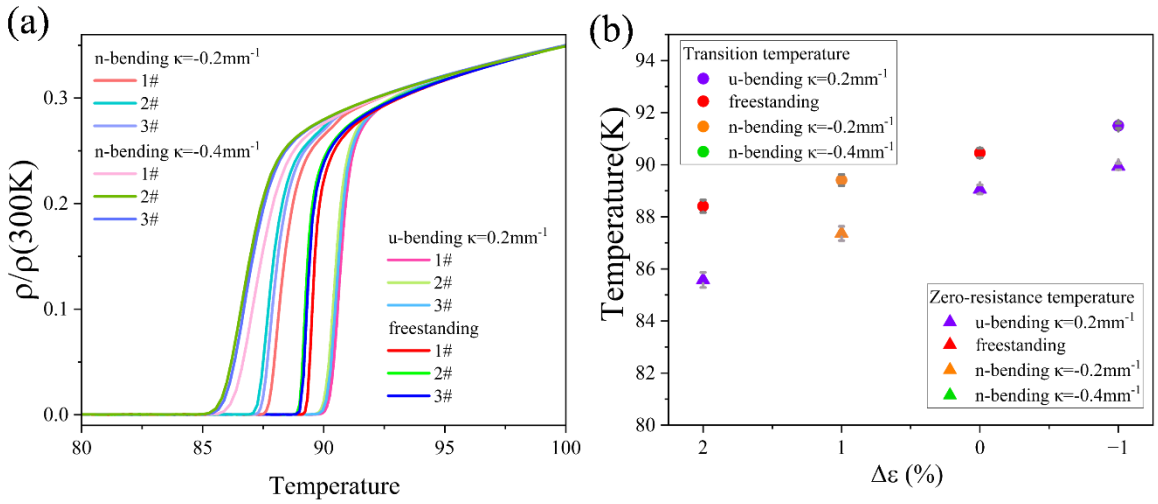

Supplementary Figure 9. Three-cycle reproducibility testing of flexible YBCO film under repeated bending. (**a**) Resistivity-temperature curves (80-100 K) under different bending conditions across three consecutive mounting-demounting cycles. (**b**) Average transition temperature Tc and zero-resistance temperature for each bending condition; error bars represent the standard deviation from three-cycle tests.

We also apply the formalism proposed by Chi Ho Wong and Rolf Lortz[59] to check if it can predict T_c of our sample in a reasonable accuracy. For bulk YBCO (x=7), we calculated a transition temperature T_c(onset) of 84 K based on the Debye temperature in the low-temperature limit. In our experiment, the film thickness is approximately 100 nm, which may be sufficient to approximate a bulk repeating unit using the experimental lattice parameters of the thin film structure. Otherwise, managing a supercell with over 1500 atoms would not be computationally feasible. For our thick YBCO(x=7) film, the antiferromagnetically enhanced d-wave electron phonon coupling (λ_{AF}) is 0.17. The charge density wave factor (R_{CDW}) is 1.4, the ARPES factor (R_{ARPES}) is 3.99. The exchange factor (f_{ex}) is 1.14. By substituting these parameters into the formalism[59], we calculated a T_c of 78 K, which is 5 K lower than the bulk value. This is consistent with our experimental results, which show that the T_c

of our thick film is 1-2 K lower than that of the bulk material.

Computation method

$YBa_2Cu_3O_7$ has been extensively documented to exhibit an isotopic effect in experimental studies. While the spin density wave does not exist in $YBa_2Cu_3O_7$, the spin density wave factor in the formalism reported by Chi Ho Wong and Rolf Lortz can be excluded in the T_c formula[59]. In this case, the formalism suggests that when electron-phonon coupling is combined with charge density wave and antiferromagnetic fluctuation together with the modified screening effect from the additional electrons slightly below the Fermi level (experimentally supported by ARPES), this interaction could enhance the coupling λ between Cooper pairs[59-62].

$$\lambda = \lambda_{AF}\, f(E_{ex})\, R_{CDW}^2\, R_{ARPES}^2$$

where λ_{AF} is the electron-phonon coupling under antiferromagnetic fluctuations in the presence of d-wave symmetry[59-62], $f(E_{ex})$ monitors the variation in antiferromagnetism under pressure, which is the ratio of the Ising Hamiltonian with respect to zero-pressure condition[59-62]. R_{CDW} represents the local change in electron concentration under a charge density wave, estimated using the two-channel model[59-62]. R_{ARPES} accounts for the screening effect from the high-energy electrons within the ARPES range, which couples with the antiferromagnetic charge density wave[59-62]. The λ is then substituted into the BCS T_c formula[59-62]. The pseudopotential μ is set to 0.1[59-62]. The ab-initio parameters used in the CASTEP calculations for the electronic, exchange, and dielectric properties are as follows[59]: For the Density Functional Theory (DFT) functional, the Generalized Gradient Approximation (GGA) with the Perdew-Burke-Ernzerhof (PBE) method was employed. The maximum number of self-consistent field (SCF) cycles allowed was set to 1000, with an SCF tolerance of approximately 2×10^{-6} eV/atom. The reciprocal k-space was defined at 0.025 (1/Å), using an ultrasoft pseudopotential and a cut-off energy of 351 eV, with a density-mixing approach[59]. In the phonon calculations, the DFT functional used was the Local Density Approximation (LDA). The cut-off radius of the supercell was set to 5 Å, with a dispersion value of 0.04 (1/Å) and the same cut-off energy of 351 eV[59]. The eigenvalue tolerance was specified as 1×10^{-9}, while the maximum SCF cycle was 100. Additionally, a smearing width of 0.1 was applied[59].

T_c calculations:

Thick film, T_c(onset)59

$\lambda = \lambda_{AF}\, f(E_{ex})\, R_{CDW}{}^2 R_{ARPES}{}^2$

$\lambda = 0.17 \times 1.14 \times 1.4^2 \times 3.99^2 = 6.05$

Renormalized $\lambda = 6.05/(6.05+1)=0.86$

$\mu=0.1$ => renormalized $\mu = 0.1/(6.05+1) = 0.014$

Given Debye temperature = 225K,

T_c(onset) = $1.13 T_{Debye} \exp(-1/(\text{Renormalized } \lambda - \text{Renormalized } \mu)$ = 78K

REFERENCES (continue)

59. C.H. Wong and R. Lortz, Unusual impact of electron-differential phonons in the modeling of the superconductivity of $YBa_2Cu_3O_x$, *iScience*, Volume 28, Issue 4, 112127 (2025)

60. C.H. Wong and R. Lortz, Phase diagram simulations incorporating the gap anisotropy with AFM spin and charge density wave under spin-orbital coupling in Fe-based superconductors, *iScience*, **27**, 110204 (2024)

61. C.H. Wong and R. Lortz, Decoding 122-type iron-based superconductors: A comprehensive simulation of phase diagrams and transition temperatures, *Phys. Rev. Research*, **6**, 013121 (2024)

62. C.H. Wong and R. Lortz, Exploring Unconventional Electron Distribution Patterns: Contrasts Between FeSe and FeSe/STO Using an Ab Initio Approach, *Materials*, 17(21), 5204 (2024)